Supporting Information

Spatially Confined Surface-Terminated MXene Nanosheets as a Multifunctional Platform for Triboelectric Sensing and Logic Gates

Rahul Mondal,[1†] Mukul Biswas,[2†] Koyendrila Debnath,[2] Snehasish Das,[3] Uday Narayan Maiti,[3] Sanat Kumar Adhikari,[4] Barun Ghosh,[2]* Avijit Chowdhury[1,2]*

[1]Technical Research Centre (TRC), S.N. Bose National Centre for Basic Sciences, JD Block, Sector III, Salt Lake, Kolkata 700106, India

[2]Department of Condensed Matter and Materials Physics, S.N. Bose National Centre for Basic Sciences, JD Block, Sector III, Salt Lake, Kolkata 700106, India

[3]Department of Physics, Indian Institute of Technology Guwahati, Guwahati 781039, Assam, India

[4]UGC-DAE CSR Kolkata Centre, Kolkata, West Bengal 700106, India

†These authors contributed equally to this work

*Corresponding author E-mail: *bghosh@bose.res.in* (B. Ghosh); *avijitc@bose.res.in (A. Chowdhury)*
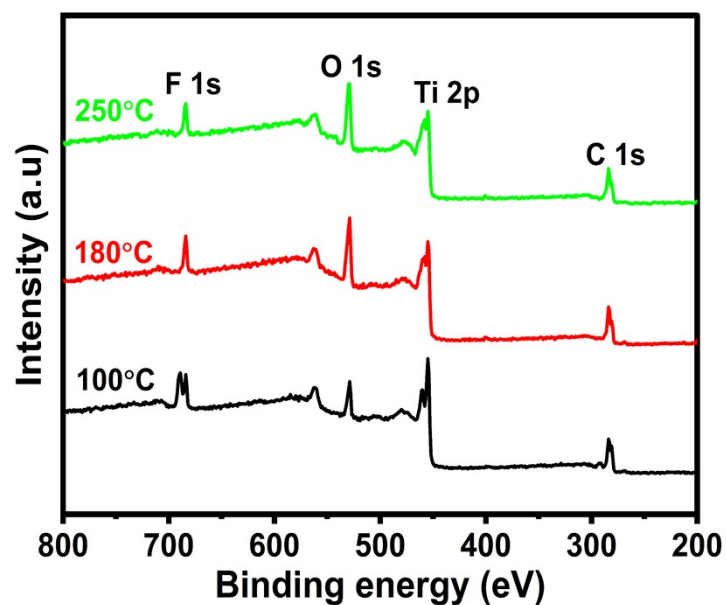
Index

Figure S1: XPS survey spectra of MXene dried at different temperatures.

Table S1

Atomic weight percentage for elements of MXene dried at different temperatures.

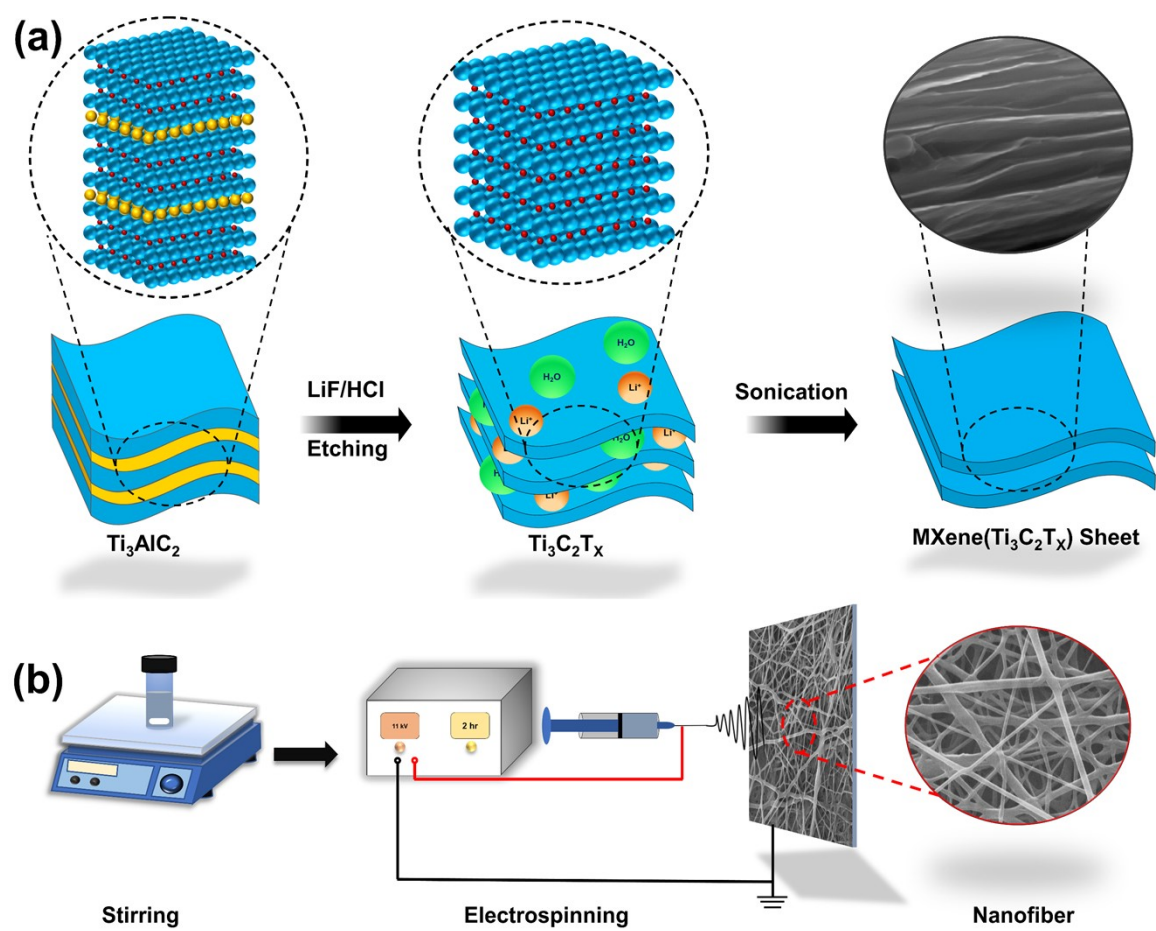| Temperature	C 1s (%)	F 1s (%)	Ti 2p (%)	O 1s (%)
100°C	39.1	23.7	21.8	15.4
180°C	42.2	23.1	17.3	17.4
250°C	43.3	19.4	16.8	20.5

Figure S2: (a) Schematic illustration of MXene preparation via in-situ chemical etching and (b) ethyl cellulose nanofiber fabrication by electrospinning processes.
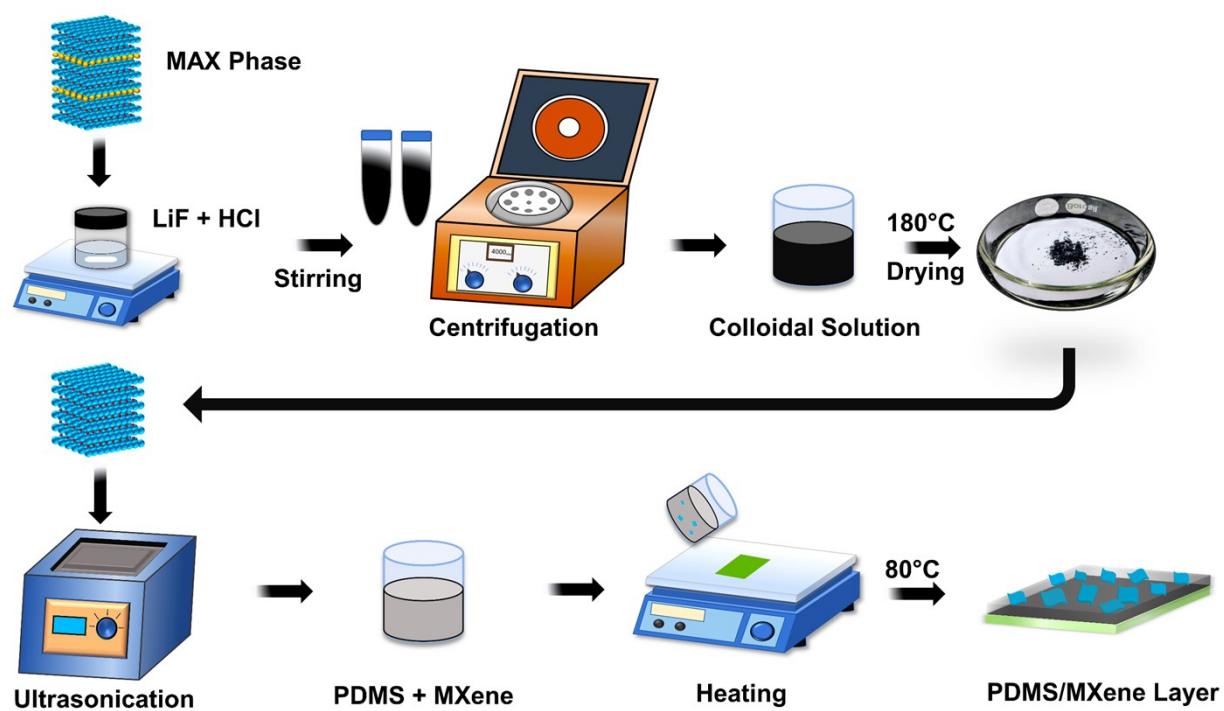
Figure S3: Schematic illustration of the PDMS/MXene composite preparation.

Supplementary Note I:

I.   The unit cell of $Ti_3C_2O_2$ monolayer

1.00000000000000

2.6458214025000002 -1.5267665239999999   0.0000000000000000

2.6458214025000002   1.5267665239999999   0.0000000000000000

0.0000000000000000   0.0000000000000000 25.0000000000000000

C   O   Ti

2   2   3

Direct

0.6667070281487872 0.6667070281487872 0.4503547360654103

0.3332929718512126 0.3332929718512126 0.5496452639345896

0.0000987761476678 0.0000987761476678 0.3616985638383536

0.9999012238523322 0.9999012238523322 0.6383014361616461

0.0000000000000000 0.0000000000000000 0.5000000000000000

0.3333377294911118 0.3333377294911118 0.3981759599605866

0.6666622705088884 0.6666622705088884 0.6018240400394135

II.   The unit cell of $Ti_3C_2F_2$ monolayer

1.00000000000000

3.0596701806235331 -0.0000000000002577   0.0000000000000000

-1.5298350902622129   2.6497521036322516   0.0000000000000000

0.0000000000000000   0.0000000000000000 25.0000000000000000

C   F   Ti

2   2   3

Direct

0.6666666866529383 0.3333333434148642 0.5511729508552494

0.3333333432161680 0.6666666864540218 0.4488270491447506

0.0000000000000000 0.0000000000000000 0.3557375397985783

0.0000000000000000 0.0000000000000000 0.6442624816414163

0.0000000000000000 0.0000000000000000 0.5000000000000000

0.3333333432161680 0.6666666864540218 0.5942685261903298

0.6666666866529383 0.3333333434148642 0.4057314523296721

III. PDMS trimer molecule with one methyl group from each of the terminal silicon atoms on both ends removed

1.00000000000000

18.3283901215000000   0.0000000000000000   0.0000000000000000

9.1713877501999992   15.8686965810000000   0.0000000000000000

0.0000000000000000   0.0000000000000000   25.0000000000000000

C   H   O   Si

10   30   4   5

Direct

0.2802806076685441 0.4521745004468216 0.7500967310127127

0.2979956534603455 0.5612228780517368 0.8387595203207743

0.2263184379978298 0.7654431661805162 0.7376208945169275

0.4926939231999117 0.2709188383185876 0.7884467038384548

0.4167343669802193 0.6643121146090942 0.7398690289221600

0.5203489486030307 0.3797135052555250 0.8723214344149706

0.7541765628603924 0.1903085681523860 0.7461224334740995

0.7407395495771351 0.3094452936294939 0.8359995187747303

0.6170921792617902 0.5295190685238083 0.7582469155686765

0.8030068167885516 0.4544598966020110 0.7349329455897263

0.2166457574462163 0.4947154353598383 0.7345262622810675

0.2745602771073830 0.4166996649634129 0.7838060994998675

0.3163453337528117 0.4065531584781783 0.7184785279134305

0.2311026528113500 0.6105037295502620 0.8377300578065967

0.1663206585826910 0.7705774762687851 0.7258179216384029

0.3053570774409922 0.5150291679885812 0.8695033346915332

0.4907397229946959 0.2588751622366517 0.7454720934591544

0.4322131583854827 0.2845314146967611 0.8062062434729088

S5

0.2311740715957860 0.7610930128809932 0.7816492993328200

0.3349534897352880 0.5904629035468880 0.8516206952683900

0.5424599860769228 0.2125642923645030 0.8068897006944550

0.2262850854272155 0.8230444382596154 0.7254934612156249

0.4201379134197630 0.6538185988284863 0.7833754863072956

0.4610661478957788 0.3973269100967155 0.8933792891263586

0.4726814079048777 0.6120043059047957 0.7217467987040264

0.4181327379804495 0.7225723422593915 0.7319391648151217

0.5708694124296024 0.3236640626420571 0.8922927286540634

0.7536117417598818 0.1514145070036861 0.7794981456698516

0.7205536889721050 0.1818787056373423 0.7125222111733371

0.7291226319287765 0.2706616585308809 0.8645956747847804

0.5336352841127987 0.4315857147124865 0.8774596728070138

0.7093380926769275 0.3743419032487118 0.8515113588361709

0.5657594101837534 0.5151128899453593 0.7582965628504205

0.8199410211380459 0.1661215778148807 0.7340599744215545

0.8091510449514669 0.2853478532851494 0.8353388581662839

0.5923800312707206 0.5959416422410592 0.7477336934212429

0.6422059157675947 0.5199612943292297 0.7992826136103507

0.8102688172338465 0.4378512259275104 0.7777625479042521

0.8594358274664867 0.4066871134950060 0.7141191111226588

0.7988049849529160 0.5160235634067935 0.7305712121180262

0.3142618981048771 0.5860938483904372 0.7280788788927018

0.4367864632977338 0.4472870192574224 0.7725265394687013

0.5996086646718675 0.3411663950433583 0.7689554416229140

0.7216879066772928 0.3596163488125063 0.7255301456363131

0.3339976223045414 0.5106851851208993 0.7716676199212912

0.3208892596691457 0.6689540695719723 0.7128177031448723

0.5126724635171979 0.3601652991441692 0.7996130807751639

0.7021702164647613 0.3020653266633679 0.7679773475808038

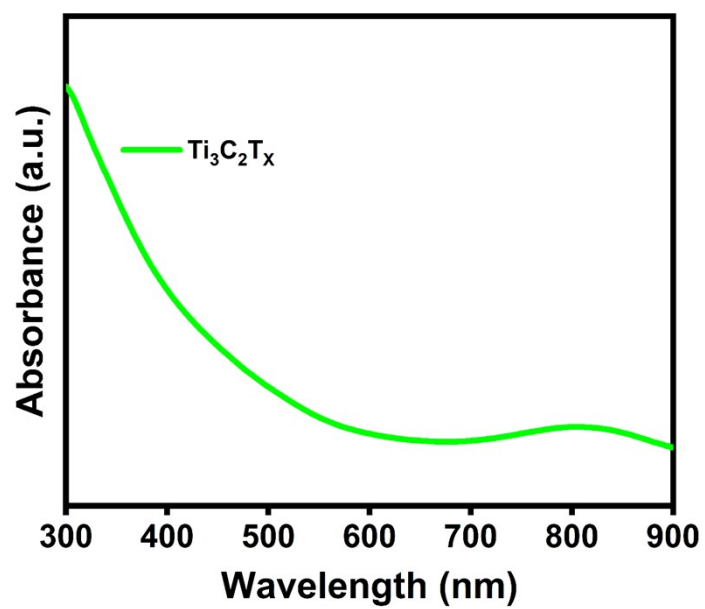0.7049392418605210 0.4549829771735471 0.7149240743057199

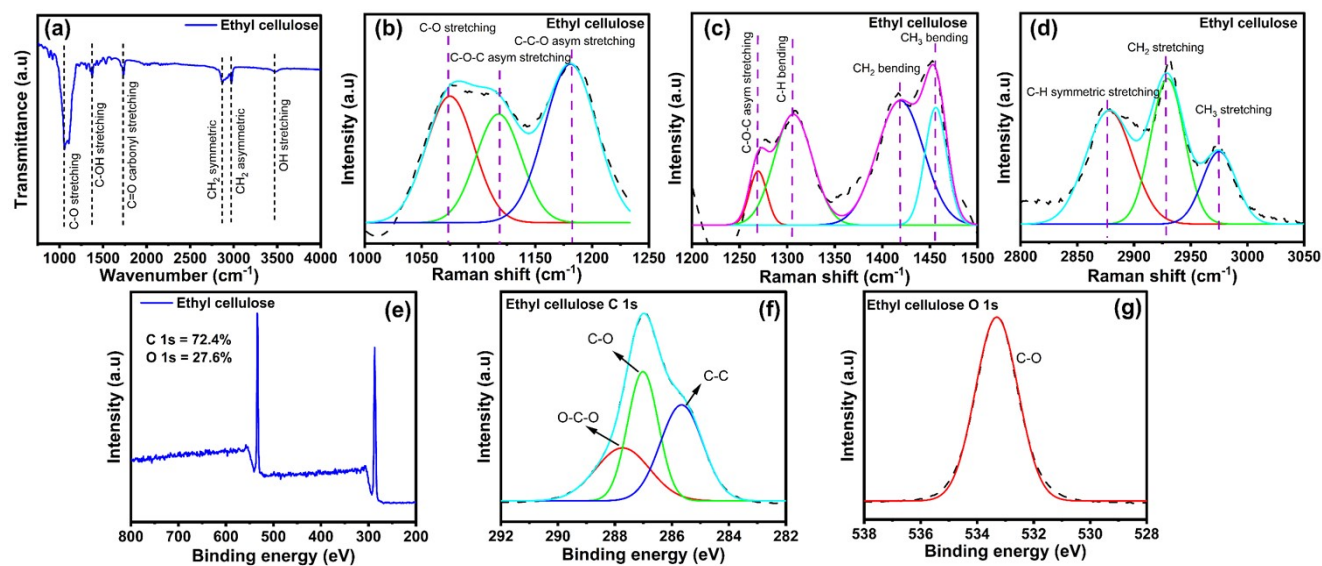**Figure S4:** UV- Visible absorption spectra of MXene**.**

Figure S5: Spectroscopic characterization of ethyl cellulose (EC): (a) FTIR spectrum, (b–d) Raman spectra, (e) XPS survey spectrum, (f) high-resolution C 1s spectrum, and (g) high-resolution O 1s spectrum.

Supplementary Note II:

The FTIR transmission spectrum is presented in **Figure S5a**. The transmittance peaks observed at 3468, 2980, 2883, 1732, 1367, and 1062 cm^{-1} correspond to O–H stretching, CH$_2$ asymmetric stretching, CH$_2$ symmetric stretching, C=O carbonyl stretching, C–OH stretching, and C–O stretching, respectively.[1] The Raman spectrum of ethyl cellulose is shown in **Figure S5b-d**. The peaks observed at 1075, 1117, 1181, 1269, 1306, 1418, 1456, 2878, 2929, and 2975 cm^{-1} are assigned to C–O stretching, C–O–C stretching, C–C–O asymmetric stretching, C–H bending, CH$_2$ bending, CH$_3$ bending, C-H symmetric stretching vibration, CH$_2$ stretching, and CH$_3$ stretching vibrations, respectively.[2] The XPS survey spectrum is shown in **Figure S5e**. For the C 1s spectrum (**Figure S5f**), the C–C, C–O, and O–C–O peaks appear at binding energies of approximately 285.0 eV, 287.0 eV, and 287.8 eV, respectively. In the O 1s spectrum (**Figure S5g**), the C–O related peak is observed at around 533.0 eV, indicating the presence of oxygen-containing functional groups.[3]
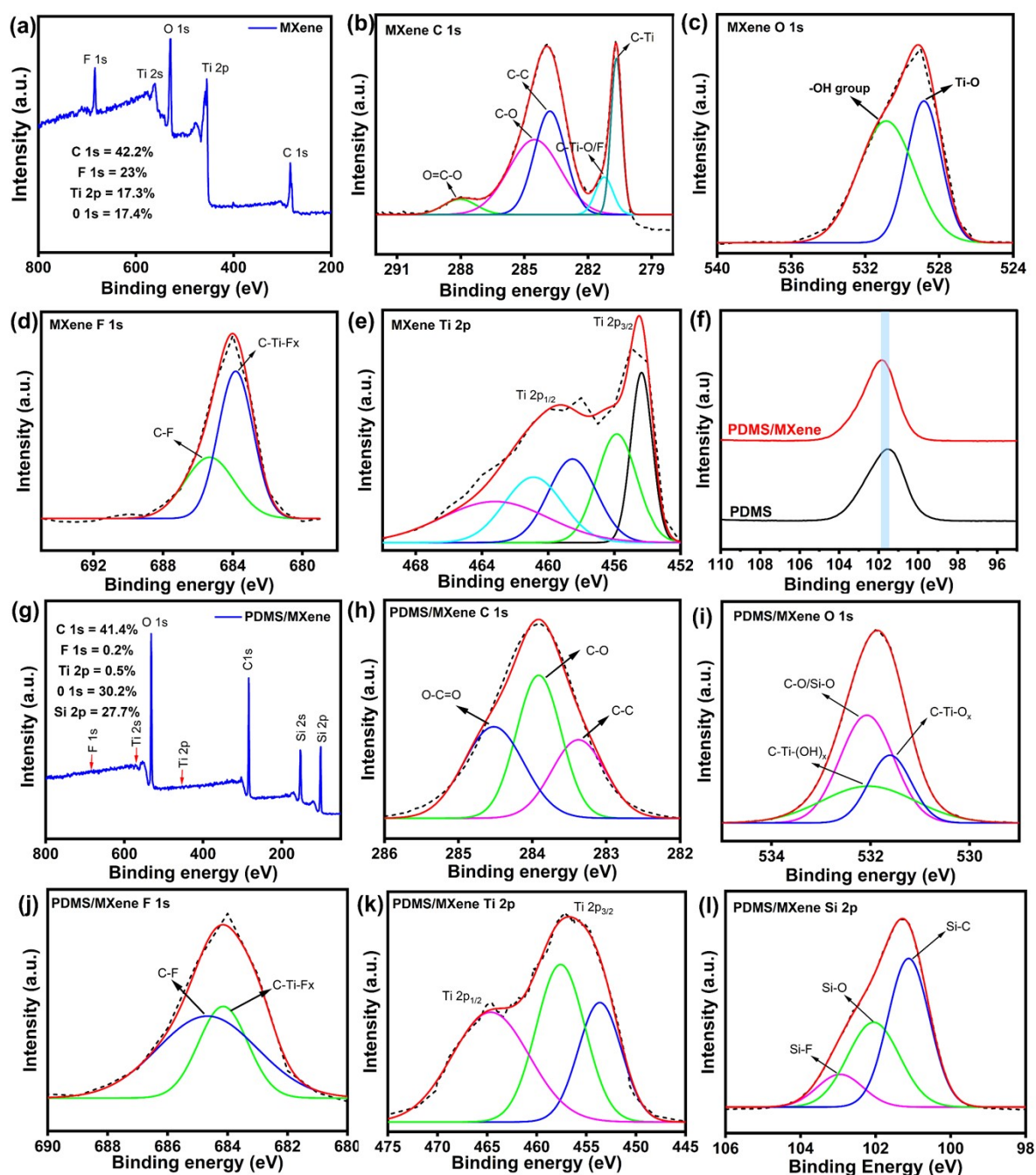
Figure S6: XPS analysis of (a-e) MXene, (f) shift of Si 2p, and (g-l) PDMS/MXene.

Supplementary Note III:

The survey spectrum of MXene, which includes F 1s, Ti 2s, O 1s, Ti 2p, and C 1s, is presented in **Figure S6a**. The high-resolution C 1s peak (**Figure S6b**) is deconvoluted into five distinct peaks at 286, 284, 283.72, 282.38, and 280.50 eV, corresponding to O–C=O, C–O, C–C, C–Ti–O/F, and C–Ti bonds, respectively.[4] The O 1s spectrum (**Figure S6c**) depicts two components at 528.8 and 530.9 eV, assigned to Ti-O and -OH groups.[5] Similarly, the F 1s spectrum (**Figure S6d**) exhibits two peaks at 685.3 and 683.8 eV, attributed to C–F and C–Ti–F_X bonds, respectively.[6] The Ti 2p spectrum (**Figure S6e**) displays spin-orbit splitting into Ti $2p_{3/2}$ (454.5 eV) and Ti $2p_{1/2}$ (459.3 eV) components.[7] The binding energy shift of Si 2p for PDMS/MXene composite towards higher binding energy confirmed the bonding between Si-F and Si-OH, as shown in **Figure S6f**. Furthermore, XPS analysis of the PDMS/MXene (**Figure S6g**) confirms the presence of characteristic MXene elements (F 1s, Ti 2s, O 1s, Ti 2p, and C 1s) alongside PDMS elements (Si 2s and Si 2p). In the PDMS/MXene, the C 1s spectrum (**Figure S6h**) contains three peaks at 284.5, 283.9, and 283.3 eV, corresponding to O-C=O, C-O, and C-C bonds, respectively. The O 1s peak of PDMS/MXene is divided into three peaks at 531.6, 532, and 532.5 eV, corresponding to C–O/Si–O, C–Ti–(OH)x, and C–Ti–Ox bonds, respectively, depicted in **Figure S6i**. The F 1s is deconvoluted into two parts at 685 and 684.1 eV, which indicates the C-Ti-F_x and C-F bond (**Figure S6j**). The Ti 2p spectrum of PDMS/MXene splits into two parts at 456.7 and 464.8 eV for Ti $2p_{3/2}$ and Ti $2p_{1/2}$, respectively, depicted in **Figure S6k**. The Si 2p peak of PDMS/MXene composites consists of two peaks at 103, 102, and 101.1 eV, which correspond to Si-F, Si–O, and Si–C bonds, respectively, as shown in **Figure S6l**.[8,9] The XPS data conclusively demonstrate the successful integration of MXene nanosheets within the PDMS matrix, evidenced by the detection of characteristic elemental signatures from both materials.
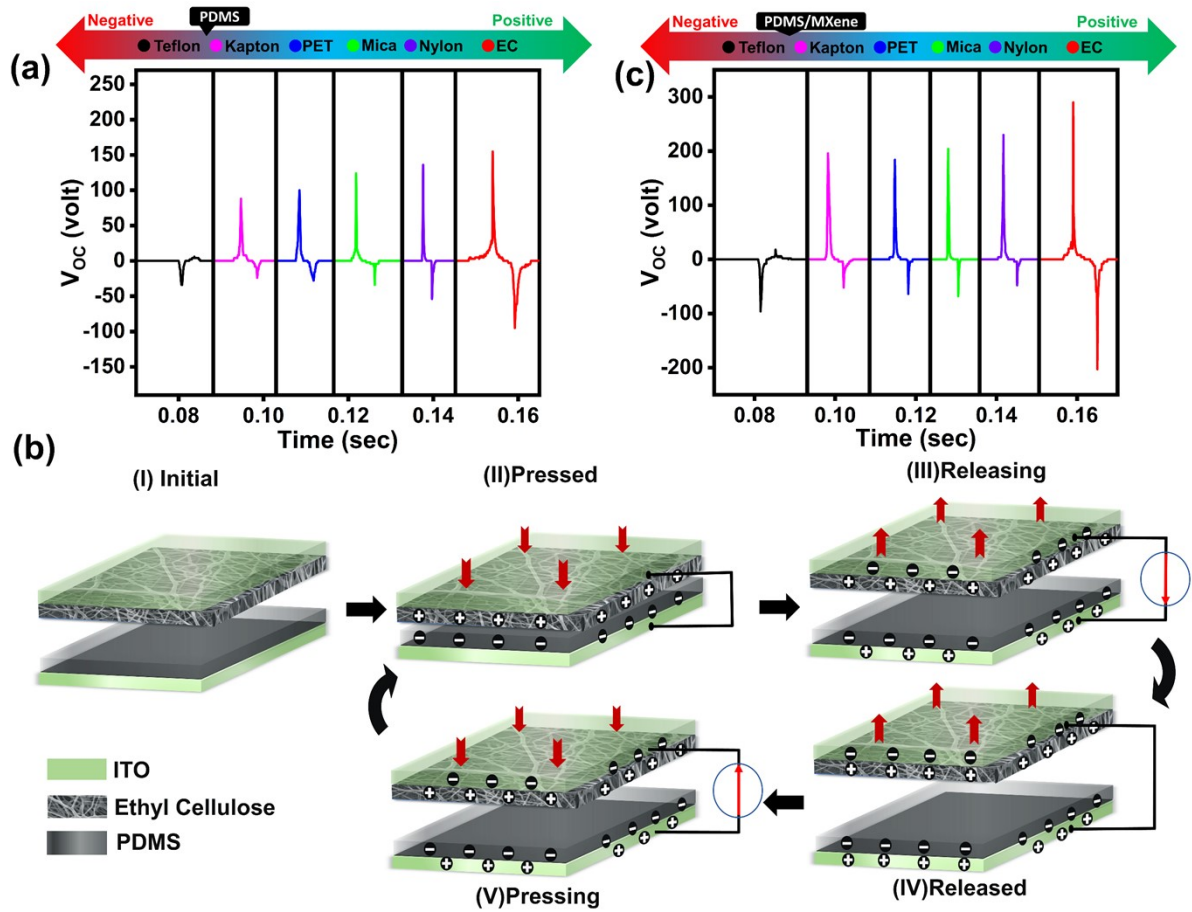
Figure S7: Tribo-output of different dielectric and working mechanism: (a) tribo-output with different dielectric and PDMS, (b) working mechanism of 'PDMS-EC' TENG, and (c) tribo-output of PDMS/MXene with different dielectric.

Supplementary Note IV:

In their initial state before contact, the triboelectric layers are electrically neutral, resulting in zero electrical potential [**Figure S7b(i)**]. Applying an external force brings the layers into contact, inducing equal and opposite surface charges. Electron transfer occurs from the EC layer to the PDMS layer, driven by PDMS's stronger electron affinity, leaving the EC surface with a net positive charge **[Figure S7b(ii)]**. As the external force is removed and the layers separate, the resulting gap creates an electrical potential difference. This potential difference drives electron flow from the PDMS electrode to the EC electrode via the external circuit, generating a transient current pulse [**Figure S7b(iii)**], with the potential reaching its peak upon complete separation [**Figure S7b(iv)**]. Subsequent compression reduces the interlayer spacing, thereby diminishing the electrical potential difference and reversing the direction of electron flow, resulting in an observed reversed current pulse [**Figure S7b(v)**]. This behaviour is consistent with PDMS acquiring a negative triboelectric charge and the EC nanofiber layer acquiring a positive triboelectric charge.
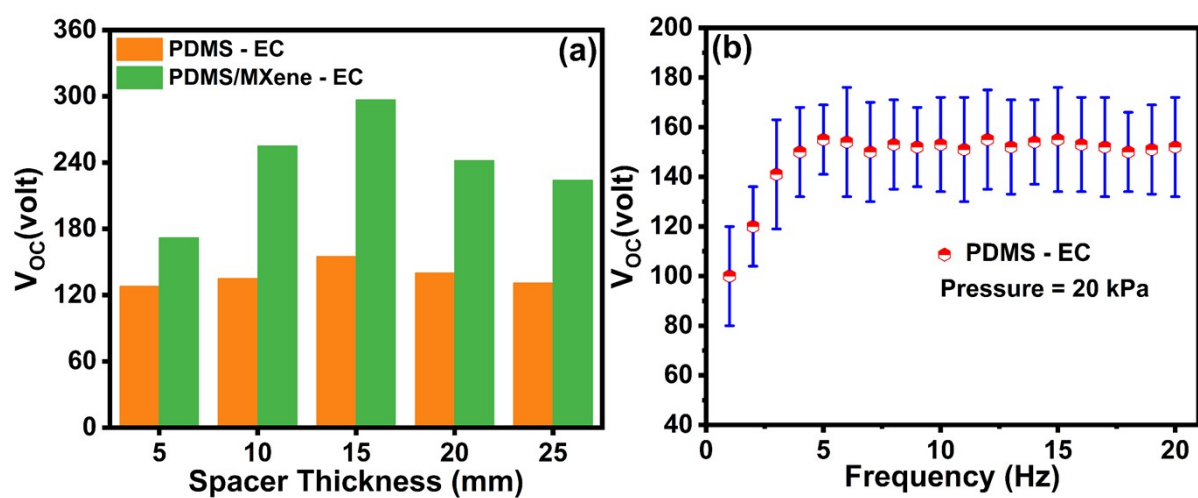
Figure S8: Open-circuit voltage of TENG with different (a) spacer thickness (frequency~ 5Hz) and (b) frequency of the applied external force.
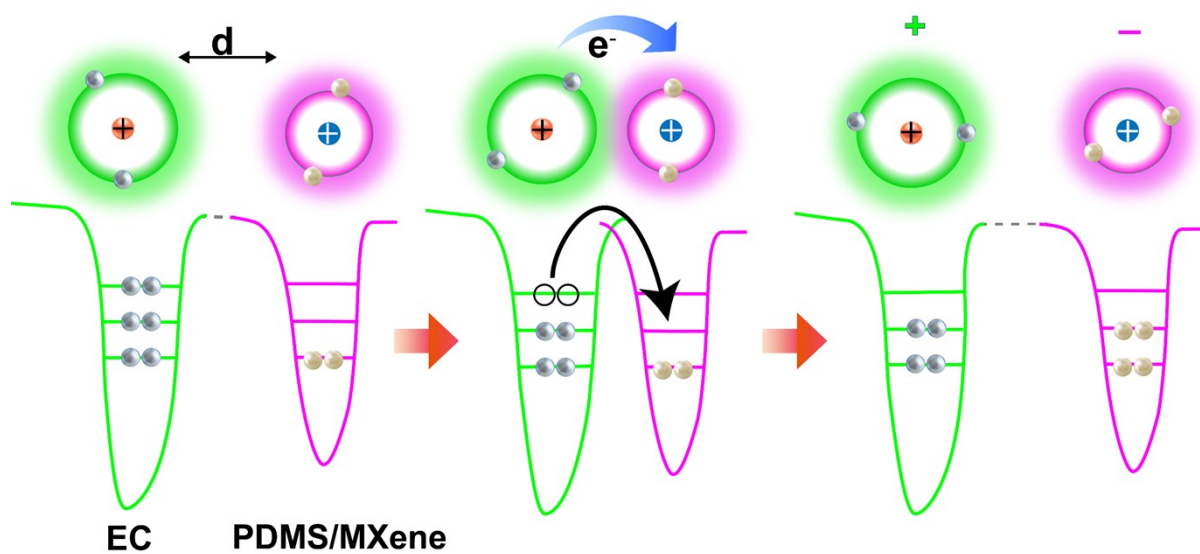
Figure S9: Electron cloud-potential well model describing contact and releasing electricfication between EC and PDMS/MXene.
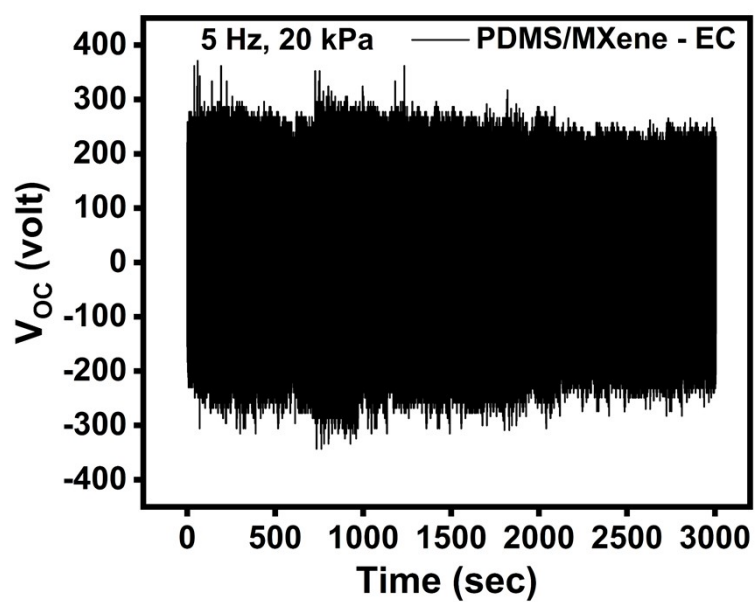
Figure S10: Long-term physical stability of PDMS/MXene-EC TENG device up to 15000 cycles.
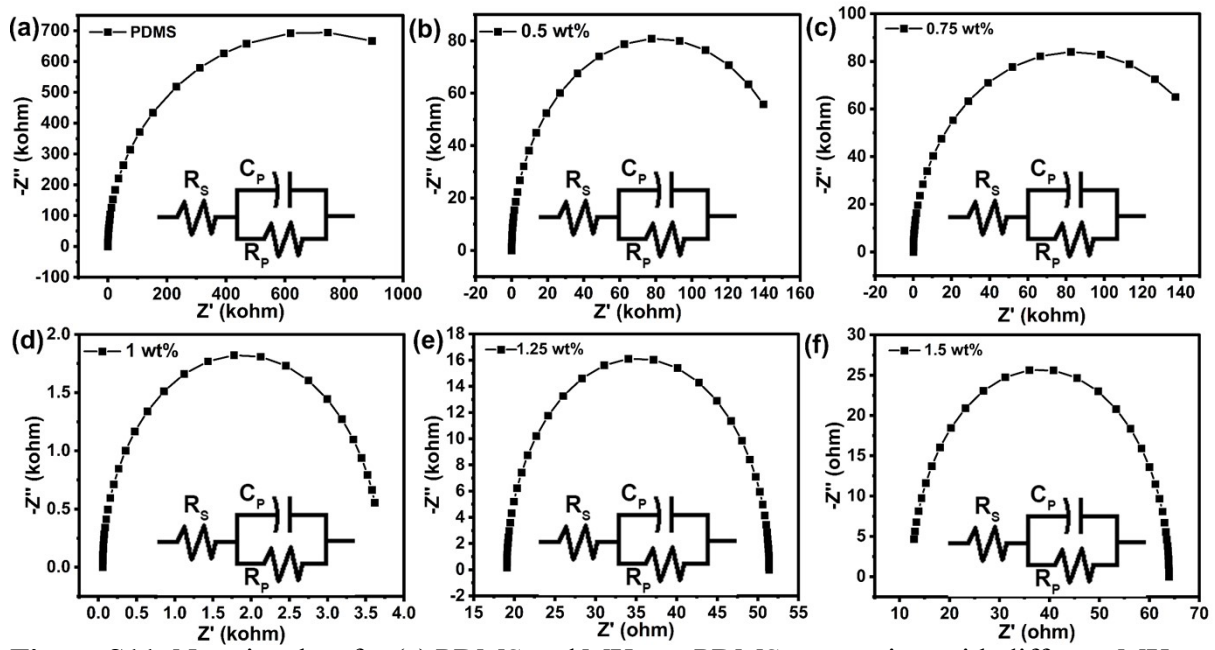
Figure S11: Nyquist plots for (a) PDMS and MXene–PDMS composites with different MXene concentrations: (b) 0.5 wt%, (c) 0.75 wt%, (d) 1 wt%, (e) 1.25 wt%, and (f) 1.5 wt%, respectively.

Table S2

Estimation of C_P and R_P values from the Nyquist plot

Sl. no	Sample name	MXene concentration (wt%)	C_P (µF)	R_P (kohm)
1	PDMS	0	0.08	14651
2	MXene-PDMS	0.5	0.89	160
3	MXene-PDMS	0.75	1.05	34.8
4	MXene-PDMS	1.00	3.20	1.6
5	MXene-PDMS	1.25	2.30	1.2
6	MXene-PDMS	1.50	1.58	1.1

.
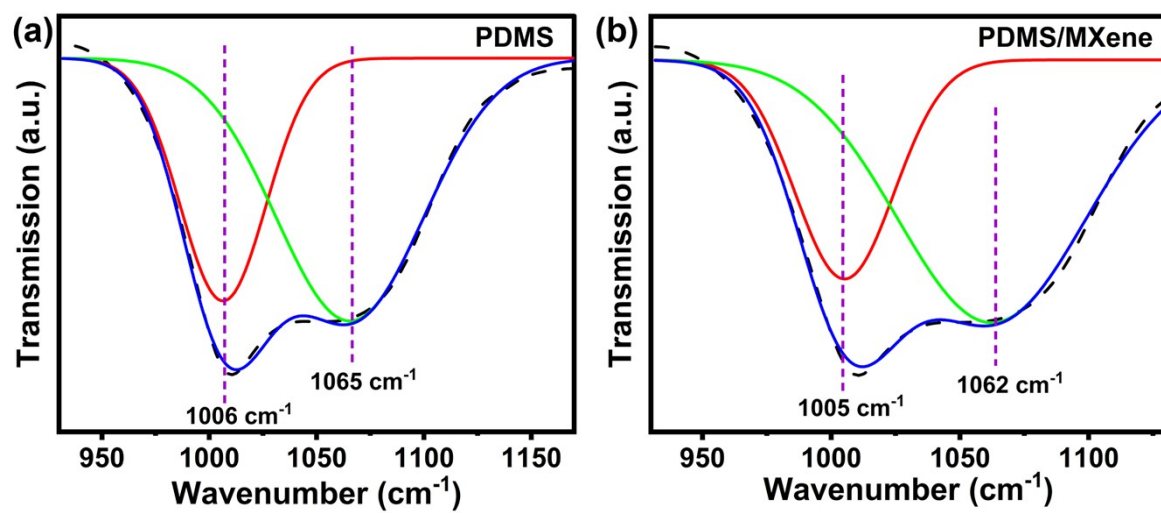
Figure S12: FTIR spectrum for Si-O-Si stretching of (a) PDMS, and (b) PDMS/MXene.
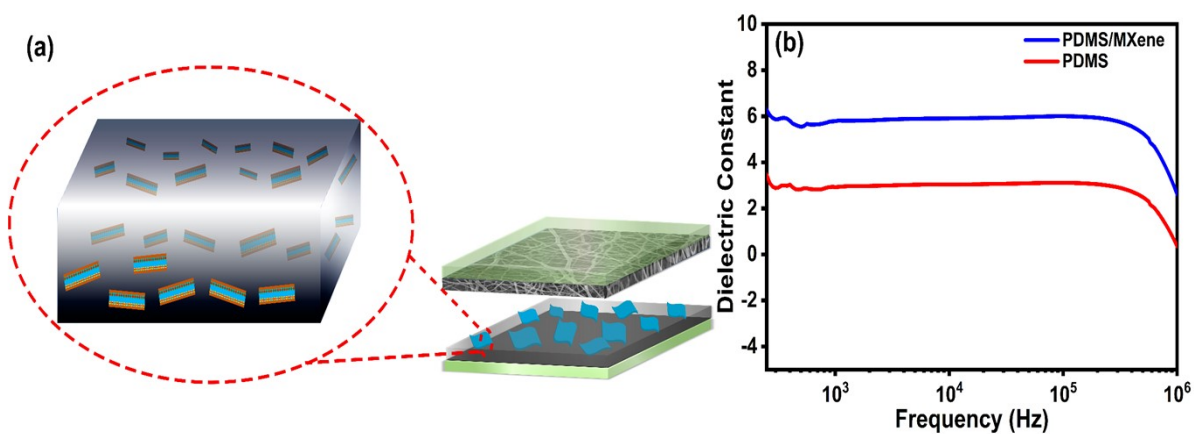
Figure S13: (a) Schematic diagram of the formation of the microcapacitor network in PDMS/MXene and (b) dielectric constant vs. frequency plot for PDMS and PDMS/MXene.
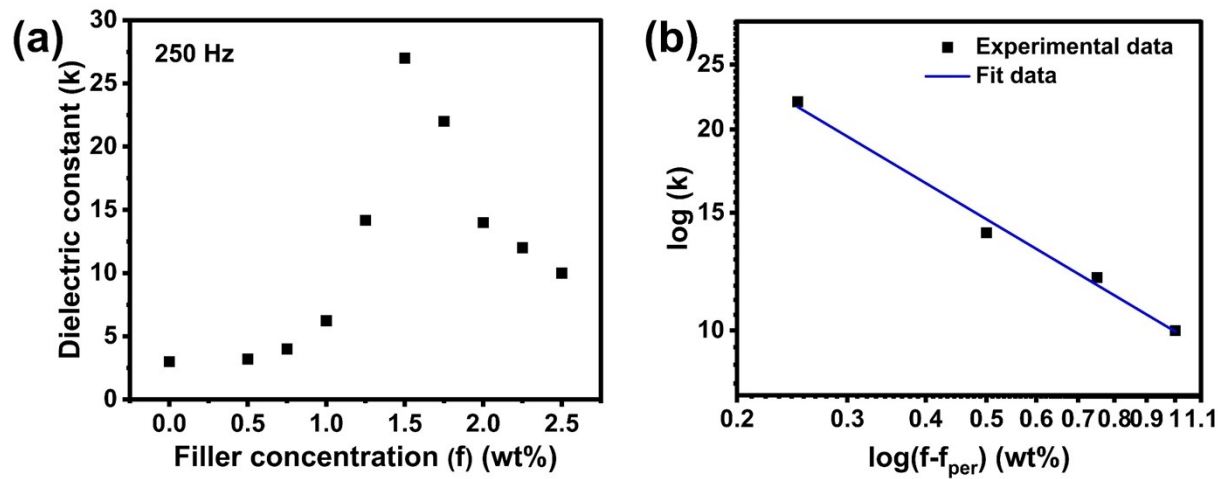
Figure S14: (a) Dielectric constant, and (b) log-log plot of dielectric constant for different filler (MXene) concentrations.
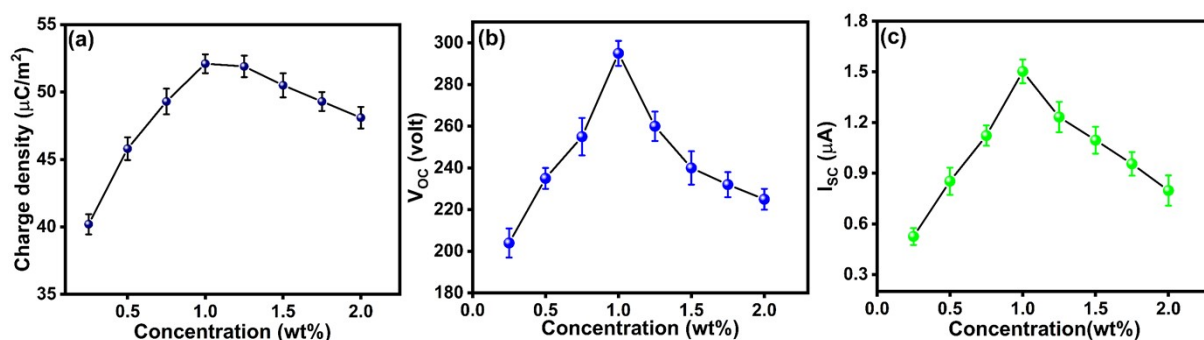
Figure S15: Tribo-performance of 'EC-PDMS/MXene' TENG for different filler (MXene) concentrations: (a) charge density, (b) open-circuit voltage, and (c) short-circuit current.
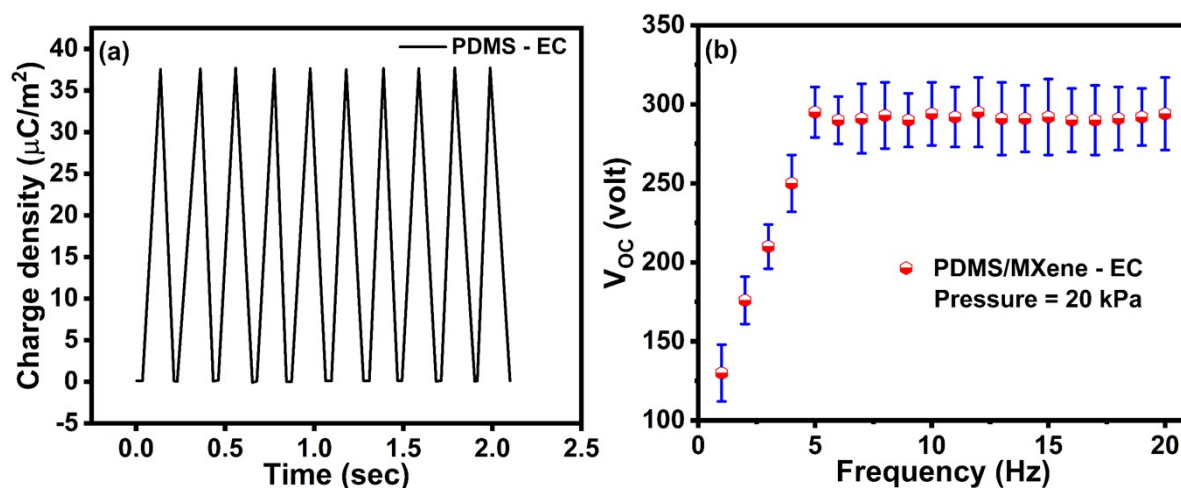
Figure S16: Estimation of (a) charge density for 'PDMS-EC' TENG, and (b) Open-circuit voltage variation with frequency for 'PDMS/MXene-EC' TENG.

Table S3

Comparative analysis of the sensitivity of TENG with previously reported work

TENG Structure	Working mode	Voltage sensitivity (V/kPa)	References
Skin/MXene	Vertical Contact separation	2.35	[10]
PTFE/PMMA	Vertical Contact separation	7.28	[11]
PVDF/PVP	Vertical Contact separation	8.80	[12]
Ecoflex/Al	Vertical Contact separation	2.57	[13]
PMMA/PDMS	Vertical contact separation	3.11	[14]
Cu/PET	Vertical contact separation	3.16	[15]
PDMS/PET	Vertical contact separation	2.82	[16]
PDMS-MXene/ EC	**Vertical contact separation**	**11.19**	**This study**
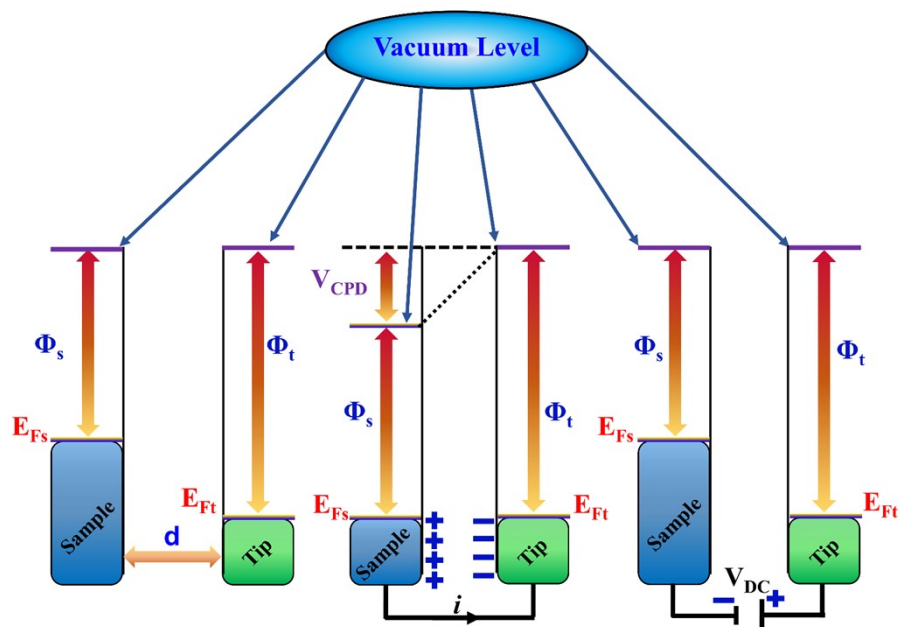
Figure S17: Schematic illustration for KPFM measurement.
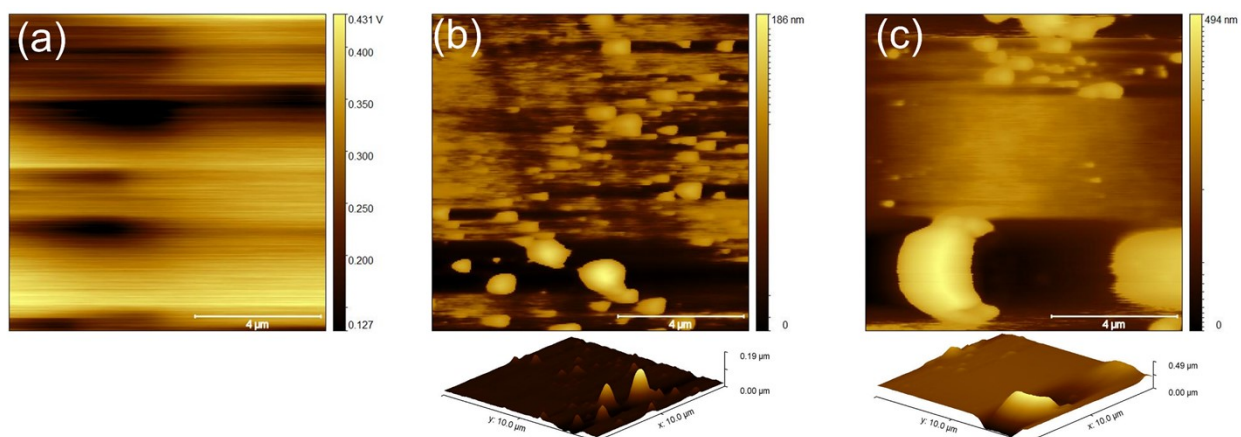
Figure S18: Surface potential of (a) PDMS, surface roughness of (b) PDMS, and (c) PDMS/MXene.
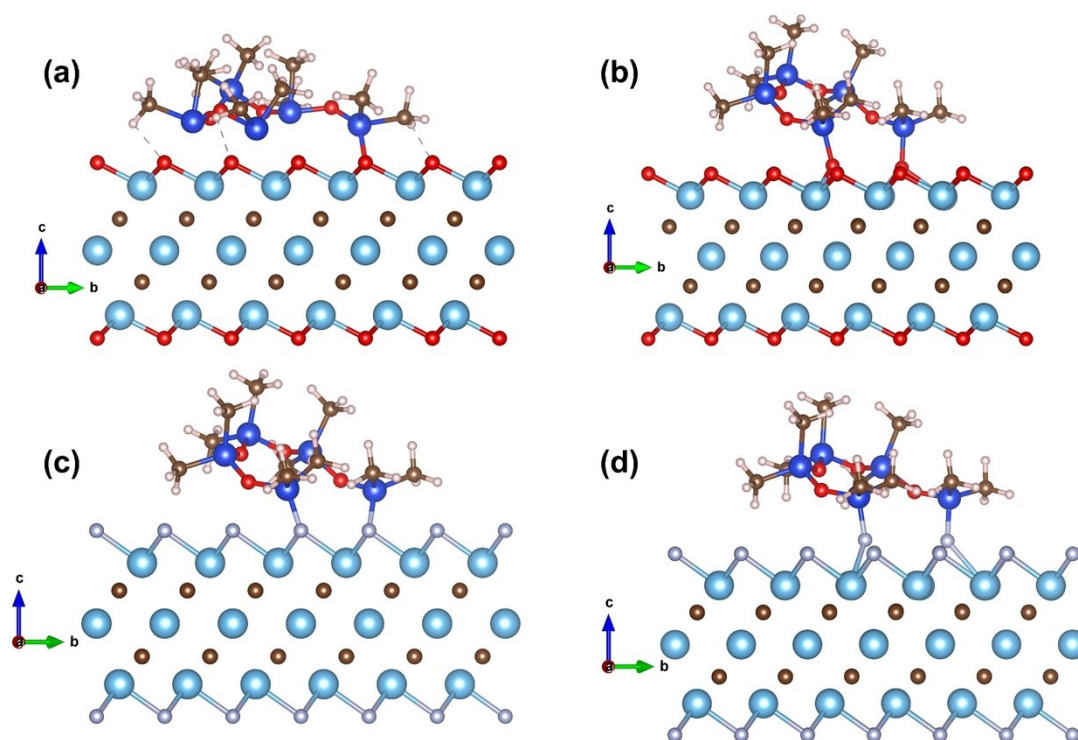
Figure S19: Unrelaxed and relaxed structures: (a, b) PDMS/Ti$_3$C$_2$O$_2$ and (c, d) PDMS/Ti$_3$C$_2$F$_2$ complexes.
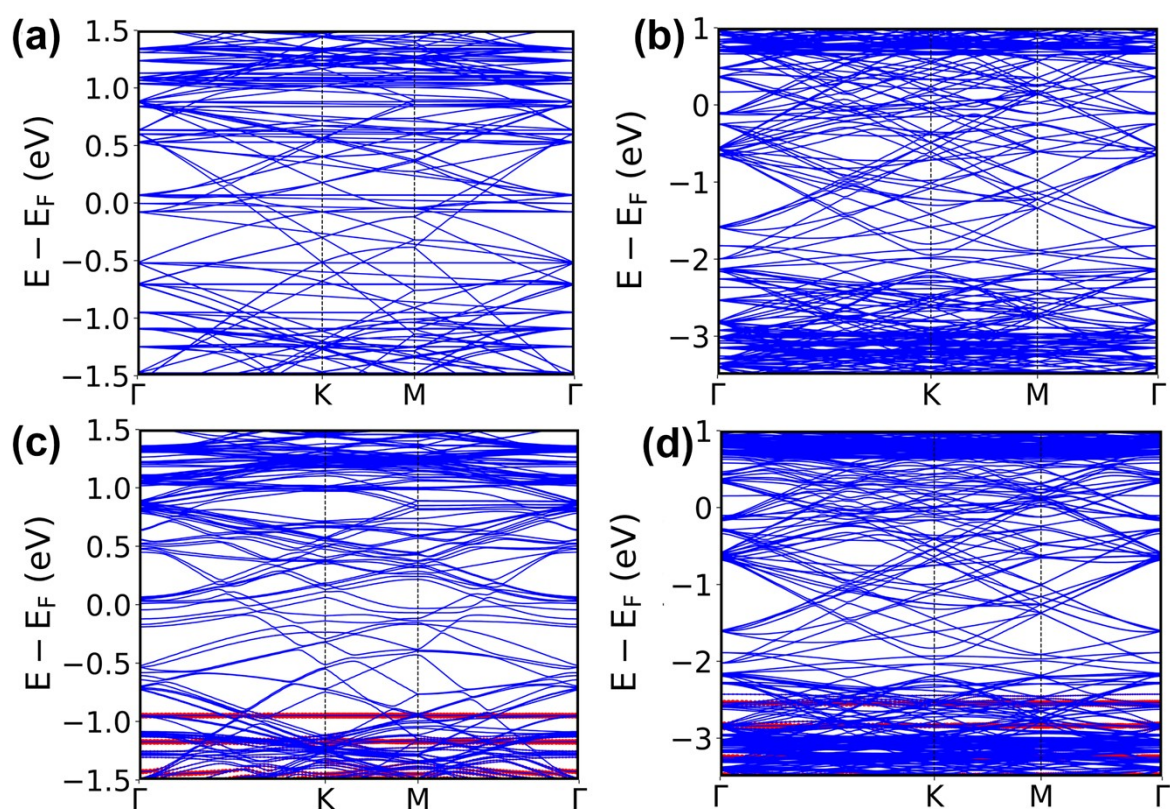
Figure S20: The electronic band structures of the 6x6x1 supercells of (a) Ti$_3$C$_2$O$_2$, (b) Ti$_3$C$_2$F$_2$, (c) PDMS on Ti$_3$C$_2$O$_2$, and (d) PDMS on Ti$_3$C$_2$F$_2$. In all the cases, the metallic nature of the

bands is evident from the plots. In the PDMS-MXene complexes, flat bands (shown in red) appear in the electronic structure, originating from the PDMS molecule.
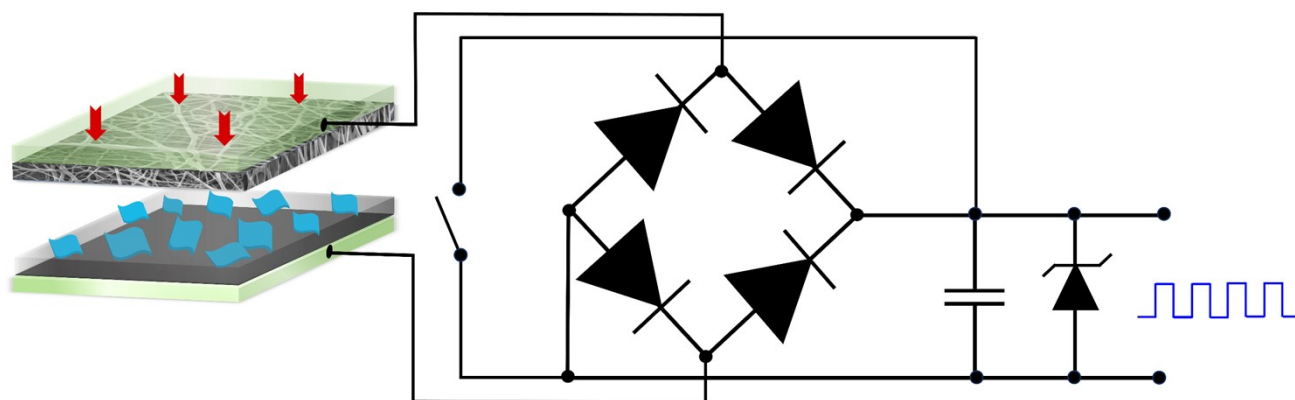
Figure S21: Circuit diagram for square waveform generation.

Supplementary Note V:

To generate a square waveform, the output of the optimized 'PDMS/MXene-EC' TENG is used as input (**Figure S21**). Firstly, the device output is rectified using a bridge rectifier and stored in a capacitor, which also helps in cancelling unwanted noise. A Zener diode is used to regulate the voltage based on its breakdown voltage. A short-circuit connection in parallel with the capacitor enables sudden discharge. The pulse width and height are adjusted by controlling the discharge time and the power rating of the Zener diode. Additionally, the peak height can be tuned by applying pressure. Higher pressure on the TENG generates a higher voltage, while lower pressure results in a lower output voltage, thereby altering the peak height.
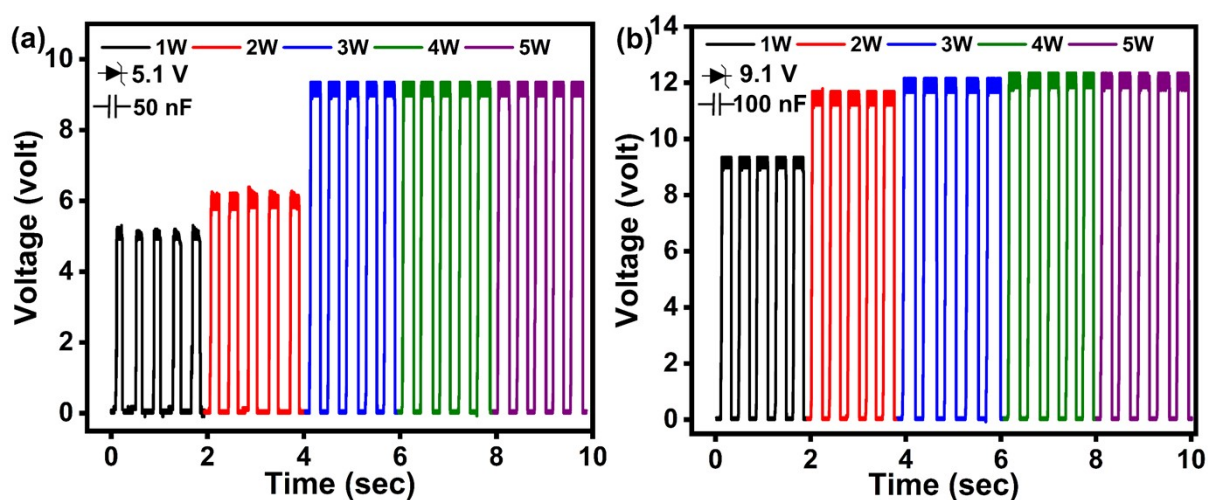
Figure S22: Generation of square waveform using Zener diodes (power rating ~ 1-5 W) and a capacitor (capacitance ~ 50 and 100 nF): (a) 5.1 V, 50 nF, and (b) 9.1V, 100nF.

Supplementary Note VI:

The electronic components, including capacitance, power rating, and Zener diode breakdown voltage, were meticulously optimized to produce a clean square waveform output. Different capacitance values, ranging from 5 nF to 200 nF, were varied to reduce noise levels. The noise level decreases as the capacitance increases. However, at higher capacitance values (100–200 nF), the charging time increases significantly, resulting in the output waveform deviating from an ideal square wave. Next, to modify the pulse height of the square wave, the breakdown voltage and power rating of the Zener diode were modulated. **Figures S22a,b** show different

square waveform heights for Zener breakdown voltages of 5.1V and 9.1V, where capacitance values of 50 nF and 100 nF, respectively, were used.

Supplementary Note VII:

To decode a binary number into its decimal equivalent, the distinct pulse on/off states of the square waveform generated by the 'PDMS/MXene-EC' TENG serve as the input for the binary digits. The absence (pulse off) and presence (pulse on) of output from the TENG represent '0' and '1', respectively. The square waveform is decoded by the ESP32 microcontroller unit and wirelessly transmitted to the smartphone via Wi-Fi. Consider the binary number '1001': the process begins by pressing the TENG device, which generates a square wave signal that is recorded as the first binary digit' 1'. The next two binary digits, '0', are automatically taken after four seconds without pressing the device. The last binary digit, '1' is recorded when the device is pressed again. To complete the decoding, a final strong press generates a pulse with a greater height than the normal pulse width. The cutoff pulse height for a normal voltage, representing binary '1', is 3V, while a pulse height of 6V signals the end of the decoding process.
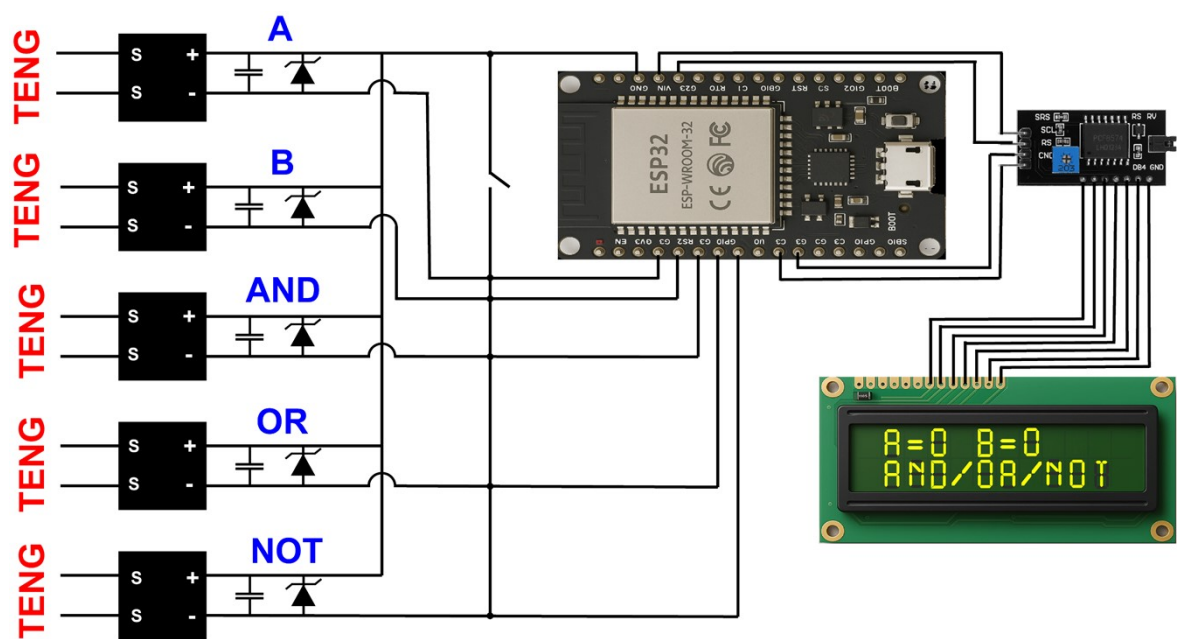
Figure S23: Schematic diagram for Boolean logic (AND, OR, NOT) operations.

Supplementary Note VIII :

Universal logic gates (AND, OR, NOT) are realized using the fabricated TENG. Here, '1' and '0' are represented as the presence (pressed) and absence (not pressed) of the square wave. Five TENGs are used to make logic gates: two for each input (A and B) and the other three for representing each logic gate (AND, OR, and NOT). For different input configurations, specific TENGs are utilized to set the corresponding values: pressing A sets A = 1 and B = 0; pressing B sets A = 0 and B = 1; and pressing both A and B sets A = 1 and B = 1. After setting each input configuration, one of the logic operations (AND, OR, or NOT) is pressed to show the corresponding result on the display.

For the AND operation, there are two inputs (A and B) and one single output (Y). The output of an AND gate is in the state 1 if and only if all the inputs assume the state 1. The Boolean expression of an AND gate having inputs denoted by A and B is written as Y= A.B. The truth table for the AND logic gate is as follows in **Table S4**.

Table S4

Inputs		Output
A	B	Y
0	0	0
1	0	0
0	1	0
1	1	1

Similarly, the output of the OR gate is in the state 1 if one or two inputs are in the state 1. The Boolean expression for the OR gate, having inputs (A and B) and the output is denoted by Y, can be written as Y = A+B. The truth table for the OR gate is shown in **Table S5**.

Table S5
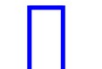
Inputs		Output
A	B	Y
0	0	0
1	1	1
0	1	1
1	1	1

Inputs		Logic	Output
A	B	⊐▷─	Y
─	─	⎍	─
⎍	─	⎍	⎍
─	⎍	⎍	⎍
⎍	⎍	⎍	⎍

Additionally, the NOT gate has a single input and a single output. The NOT logic is in the state 1 if and only if the input does not assume the state 1. The output of the logic is high when the input is low, and vice versa. The Boolean algebra for input A and Y can be written as, $Y = \bar{A}$. The truth table for the NOT gate is shown in **Table S6**. By carefully designing switching circuits controlled by TENG's high and low voltage states, the behavior of universal gates, such as NAND or NOR, can also be implemented (not shown here).

Table S6

Inputs	Output
A	Y
0	1
1	0

Inputs	Logic	Output
A	▶●─	Y
─	⎍	─
⎍	⎍	⎍

Video Link S1 (binary to decimal):

https://drive.google.com/file/d/1IU0AmTkPSyEc2BuJ2zGtOq1ulnNvCBZW/view?usp=sharing

Video Link S2 (LED):

https://drive.google.com/file/d/1DXoRpq_QEx3XvDmk350bTCWbr0XC5Om3/view?usp=sharing

Video Link S3 (Logic gates):

https://drive.google.com/file/d/1EUgNeO9QQ575hWOPS413frMRKZ126l-r/view?usp=sharing

References:

1 K. K. Khichar, S. B. Dangi, V. Dhayal, U. Kumar, S. Z. Hashmi, V. Sadhu, B. L. Choudhary, S. Kumar, S. Kaya, A. E. Kuznetsov, S. Dalela, S. K. Gupta and P. A. Alvi, *Polymer Composites*, 2020, **41**, 2792–2802.

2 J. Rohowsky, K. Heise, S. Fischer and K. Hettrich, *Carbohydrate Polymers*, 2016, **142**, 56–62.

3 M. H. Abdellah, L. Pérez-Manríquez, T. Puspasari, C. A. Scholes, S. E. Kentish and K. Peinemann, *Advanced Sustainable Systems*, 2018, **2**, 1800043.

4 O. B. Seo, S. Saha, N. H. Kim and J. H. Lee, *Journal of Membrane Science*, 2021, **640**, 119839.

5 A. Tanvir, P. Sobolčiak, A. Popelka, M. Mrlik, Z. Spitalsky, M. Micusik, J. Prokes and I. Krupa, *Polymers*, 2019, **11**, 1272.

6 W. Xu, S. Li, W. Zhang, B. Ouyang, W. Yu and Y. Zhou, *ACS Appl. Mater. Interfaces*, 2021, **13**, 49242–49253.

7 L.-Å. Näslund, P. O. Å. Persson and J. Rosen, *J. Phys. Chem. C*, 2020, **124**, 27732–27742.

8 X. Su, W. Yang, Z. Zhang, L. Deng, K. Li, H. Xie, Y. Wu, X. Zhang and W. Wu, *ACS Appl. Nano Mater.*, 2024, **7**, 2164–2175.

9 Y.-J. Oh, S. M. Cho and C.-H. Chung, *J. Electrochem. Soc.*, 2005, **152**, C348.

10 Y. Cao, Y. Guo, Z. Chen, W. Yang, K. Li, X. He and J. Li, *Nano Energy*, 2022, **92**, 106689.

11 A. A. Jan, S. Kim and S. Kim, *Soft Sci*, DOI:10.20517/ss.2023.54.

12 C. Garcia, I. Trendafilova, R. Guzman De Villoria and J. Sanchez Del Rio, *Nano Energy*, 2018, **50**, 401–409.

13 A. Aamir Jan, S. Kim and S. Kim, *Soft Matter*, 2024, **20**, 6558–6567.

14 K. Ke and C. Chung, *Small*, 2020, **16**, 2001209.

15 G. Min, A. Singh Dahiya, D. M. Mulvihill and R. Dahiya, in *2021 IEEE International Conference on Flexible and Printable Sensors and Systems (FLEPS)*, IEEE, Manchester, United Kingdom, 2021, pp. 1–4.

16 X.-Z. Jiang, Y.-J. Sun, Z. Fan and T.-Y. Zhang, *ACS Nano*, 2016, **10**, 7696–7704.